PRECLINICAL TRANSGENIC AND PATIENT-DERIVED XENOGRAFT MODELS RECAPITULATE THE RADIOLOGICAL FEATURES OF HUMAN ADAMANTINOMATOUS CRANIOPHARYNGIOMA

Jessica K. R. Boult[1], John R. Apps[2], Annett Hölsken[3], J. Ciaran Hutchinson[4], Gabriela Carreno[2], Laura S. Danielson[5], Laura M. Smith[5], Tobias Bäuerle[6], Rolf Buslei[3,7], Michael Buchfelder[8], Alex K. Virasami[4], Alexander Koers[5], Owen J. Arthurs[4], Thomas S. Jacques[2,4], Louis Chesler[5], Juan Pedro Martinez-Barbera[2], Simon P. Robinson[1]

[1] Division of Radiotherapy and Imaging, The Institute of Cancer Research, London, UK.

[2] Developmental Biology and Cancer Programme, Birth Defects Research Centre, UCL Great Ormond Street Institute of Child Health, University College London, London, UK.

[3] Department of Neuropathology, University Hospital Erlangen, Friedrich-Alexander University Erlangen-Nürnberg, Erlangen, Germany.

[4] Histopathology Department, Great Ormond Street Hospital for Children NHS Foundation Trust, London, UK.

[5] Division of Clinical Sciences, The Institute of Cancer Research, London, UK.

[6] Institute of Radiology, Preclinical Imaging Platform Erlangen (PIPE), University Hospital Erlangen, Friedrich-Alexander-Universität Erlangen-Nürnberg, Erlangen, Germany

[7] Institute of Pathology, Sozialstiftung Bamberg, Bamberg, Germany

[8] Department of Neurosurgery, University Hospital Erlangen, Friedrich-Alexander University Erlangen-Nürnberg, Erlangen, Germany.

Corresponding author: Dr Jessica Boult

Division of Radiotherapy and Imaging

The Institute of Cancer Research,

London

SM2 5NG, UK

Telephone: +44 (0)208 722 4699

Email: Jessica.Boult@icr.ac.uk

Abstract

Aim: To assess the clinical relevance of transgenic and patient-derived xenograft models of adamantinomatous craniopharyngioma (ACP) using serial magnetic resonance imaging (MRI) and high resolution post-mortem micro-computed tomography (μ-CT), with correlation with histology and human ACP imaging.

Methods: The growth patterns and radiological features of tumours arising in $Hesx1^{Cre/+};Ctnnb1^{lox(ex3)/+}$ transgenic mice, and of patient-derived ACP xenografts implanted in the cerebral cortex, were monitored longitudinally *in vivo* with anatomical and functional MRI, and by *ex vivo* μ-CT at study end. Pathological correlates with haematoxylin and eosin stained sections were investigated.

Results: Early enlargement and heterogeneity of $Hesx1^{Cre/+};Ctnnb1^{lox(ex3)/+}$ mouse pituitaries was evident at initial imaging at 8 weeks, which was followed by enlargement of a solid tumour, and development of cysts and haemorrhage. Tumours demonstrated MRI features that recapitulated those of human ACP, specifically, T_1-weighted signal enhancement in the solid tumour component following Gd-DTPA administration, and in some animals, hyperintense cysts on FLAIR and T_1-weighted images. *Ex vivo* μ-CT correlated with MRI findings and identified smaller cysts, which were confirmed by histology. Characteristic histological features, including wet keratin and calcification, were visible on μ-CT and verified by histological sections of patient-derived ACP xenografts.

Conclusions: The $Hesx1^{Cre/+};Ctnnb1^{lox(ex3)/+}$ transgenic mouse model and cerebral patient-derived ACP xenografts recapitulate a number of the key radiological features of the human disease and provide promising foundations for *in vivo* trials of novel therapeutics for the treatment of these tumours.

Introduction

Adamantinomatous craniopharyngioma (ACP) is the most common tumour of the sellar region in childhood, accounting for approximately 1.2-4% of paediatric intracranial tumours. Peak incidence occurs at 5-9 years with a second peak in adults aged 45-60 years (20, 21). Although appearing histopathologically benign and classified by the World Health Organisation as grade I (17), ACP is often clinically aggressive, demonstrating invasion of the hypothalamus and visual pathways, and destruction of the pituitary. Current treatment strategies involve surgery, radiotherapy and cystic drainage. Although associated with good 5 year survival, patients frequently suffer severe long term morbidity, with pituitary and hypothalamic dysfunction, visual impairment and poor quality of life (20).

ACP is an epithelial lesion thought to arise from Rathke's pouch, the embryonic primordium of the anterior pituitary, and is characterised by the formation of a peripheral basal layer of palisading epithelium, loose aggregates of stellate cells, nodules of "wet keratin" (anuclear 'ghost cells'), whorl-like cell clusters and cysts containing high levels of protein, cholesterol and calcification (19). ACPs present as variably cystic/solid tumours in the intrasellar and/or suprasellar region by both magnetic resonance imaging (MRI) and computed tomography (CT) (10). Calcification, present in over 90% of ACPs, is detectable by CT, which is therefore widely used for differential diagnosis following initial identification by MRI (29).

Mutations in *CTNNB1*, which encodes β-catenin, predicted to cause the over-activation of the WNT pathway, have been identified in the majority of human ACP samples analysed (7, 9, 15, 24). Unusually, nuclear-cytoplasmic localisation of activated β-catenin is found in only a small proportion of tumour cells, either as small cell clusters, which broadly correlate with epithelial whorls, or otherwise dispersed in a minority of cells throughout the tumour (9, 11). We have

recently described the 3D structure of human ACP using high resolution micro-CT (μ-CT) imaging (2), and corroborated the presence of clusters at the leading invasive edge of tissue invasion (8, 26).

Expression of oncogenic β-catenin in the developing pituitary in $Hesx1^{Cre/+};Ctnnb1^{lox(ex3)/+}$ mice results in tumours resembling human ACP at the histological and molecular levels (11). Despite activation of β-catenin in all pituitary cells in this model, nuclear accumulation is only observed in small clusters of cells, analogous to human clusters. Previous studies have shown that these mice have a median survival of approximately 11 weeks, with a remarkable variability, and at the time of death exhibit large cystic masses beneath the brain (11). To date, the kinetics of tumour development in this transgenic mouse model of ACP has not been studied.

A patient-derived xenograft model of ACP has also been established through placement of uncultivated human tumour tissue into the cerebral hemisphere of immunodeficient mice (26). Lesions propagated in this manner show comparable tissue architecture and express similar immunohistochemical markers to the patient tumours, including whorl-like cell clusters with nuclear β-catenin accumulation and activated EGFR (26).

In this study we have further characterised tumours arising in the $Hesx1^{Cre/+};Ctnnb1^{lox(ex3)/+}$ transgenic mouse model of ACP *in vivo*, describing both their radiological features and patterns of growth through longitudinal multiparametric MRI imaging. Using μ-CT we have assessed both these murine tumours, and cerebral patient-derived ACP xenografts, *ex-vivo* in 3D at high resolution. Comparison with clinical imaging and pathology demonstrated that both these models recapitulate the radiological features of human ACP.

Materials and Methods

Hesx1$^{Cre/+}$;Ctnnb1$^{lox(ex3)/+}$ transgenic model of ACP

Hesx1$^{Cre/+}$;Ctnnb1$^{lox(ex3)/+}$ mice have been described previously (11). All experiments were performed in accordance with the local Animal Welfare and Ethical Review Board, the UK Home Office Animals (Scientific Procedures) Act 1986, the United Kingdom National Cancer Research Institute guidelines for the welfare of animals in cancer research (30) and the ARRIVE (animal research: reporting *in vivo* experiments) guidelines (16). Eighteen *Hesx1$^{Cre/+}$;Ctnnb1$^{lox(ex3)/+}$* and four wildtype control mice were assessed in this study.

Patient-derived ACP xenograft model

A fresh surgical specimen from a 56 year old male patient with ACP was retrieved from the Department of Neurosurgery at the University Hospital Erlangen. Tumour tissue was verified and classified as previously and was found to bear a TCT(Ser)>TGT(Cys) mutation in codon 33 of *CTNNB1* but no mutation in exon 15 of *BRAF* (13, 26). A declaration of consent for the patient is available, approved by the local ethics committee of the Friedrich-Alexander-Universität Erlangen-Nürnberg. Procedures were conducted in accordance to the Declaration of Helsinki.

All experiments performed were authorised by the local government (Regierung von Unterfranken, Germany, Ref.-No. 54-2532.01-25/14) in accordance with the animal protection act. The surgical specimen was divided and implanted into the right cerebral hemisphere of four female NMRI-Fox1^{nu}/Fox1^{nu} mice (Janvier Labs, Le Genest-Saint-Isle, France). Anaesthetised mice were secured in a stereotactic frame (Bilaney Consultants, Düsseldorf, Germany), a 5mm incision made in the scalp and a 1mm burr hole drilled 3mm lateral to the bregma. A piece of uncultivated tumor tissue (1–8mm^3) was inserted through the hole using a sterile cannula and the skin closed using a suture (ETHILON*II 4-0, Ethicon, Norderstedt, Germany). Analgesic (1mg/g metamizole, Ratiopharm,

Ulm, Germany) was added to the drinking water for 3 days following the procedure. Body weight and animal behaviour were monitored daily (26).

Magnetic resonance imaging

^{1}H MRI of *Hesx1$^{Cre/+}$;Ctnnb1$^{lox(ex3)/+}$* mice was performed on a 7T horizontal bore microimaging system (Bruker, Ettlingen, Germany) using a 30mm birdcage coil and 1mm thick slices acquired over a 25mm x 25mm field of view (FOV). Imaging was performed fortnightly from approximately 8 weeks of age, increasing to weekly once tumour progression was established. Anaesthesia was induced with either 3% isoflurane in 100% oxygen (1L/min) and maintained with 1% isoflurane (for longitudinal screening/monitoring), or a 10ml/kg intraperitoneal injection of fentanyl citrate (0.315mg/ml) plus fluanisone (10mg/ml (Hypnorm; Janssen Pharmaceutical Ltd. High Wycombe, UK)), midazolam (5mg/ml (Hypnovel; Roche, Burgess Hill, UK)), and sterile water (1:1:2) (for functional MRI at study end). A lateral tail vein was cannulated with a 27G butterfly catheter (Venisystems, Hospira, Royal Leamington Spa, UK) if remote administration of Gd-DTPA (Magnevist™; Schering, Berlin, Germany) was required. Core body temperature was maintained by warm air blown through the magnet bore.

Magnetic field homogeneity was first optimised by shimming over the entire brain using an automated shimming routine (FASTMAP). Anatomical multi-slice contiguous T$_2$-weighted RARE images (T$_R$=4500ms, T$_E$eff=36ms, 8 averages, 256x256 matrix, pixel size=98μmx98μm) were then acquired to monitor tumour development and for subsequent volumetric analysis. Fluid attenuated inversion recovery (FLAIR; T$_R$=18000ms, T$_E$eff=35ms, T$_I$=2100ms, 4 averages, flip angle=125°, 128x128 matrix) and T$_1$-weighted (T$_R$=1300ms, T$_E$=7.5ms, 4 averages, RARE factor=8, 256x256 matrix) images were also acquired. At study end, echo-planar diffusion-weighted imaging (EPI-DWI) was used to determine the apparent diffusion coefficient (ADC) (5), and either T$_1$-weighted images acquired before and 1 minute after intravenous administration of 0.1mmolkg^{-1} Gd-DTPA

(Magnevist, Schering), or dynamic contrast-enhanced (DCE) MRI (4) was used to assess patent tumour vasculature.

MRI of nude mice bearing cerebral patient-derived ACP xenografts was performed between 124 and 130 days after tumour implantation, at which time successful tumour engraftment had previously been confirmed histologically (26), under isoflurane anaesthesia, on a 7T horizontal bore microimaging system (Bruker, Ettlingen, Germany) equipped with a dedicated mouse brain coil and an animal monitoring system. T_2-weighted images (T_R=2370ms, T_E=41ms, slice thickness=0.7mm, FOV=24mmx38mm, 210x320 matrix, pixel size=119μmx119μm) and T_1-weighted contrast-enhanced images prior to and following intravenous administration of 0.1mmolkg^{-1} gadobutrol (Gadovist, Bayer Vital, Leverkusen, Germany) (T_R=500ms, T_E=9ms, slice thickness=0.7mm, FOV=24mmx28mm, 448x512 matrix, pixel size=55μmx55μm) were acquired.

MRI data analysis

Volumetric analysis was performed using segmentation from regions of interest (ROIs) drawn on T_2-weighted images. Parameter estimation was undertaken using a Bayesian maximum *a posteriori* algorithm, which took into account the Rician distribution of noise in magnitude MR data in order to provide unbiased parameter estimates (27, 28). Estimates of the ADC (x10^{-6}mm^{2}s^{-1}) were determined from the EPI-DWI data. DCE MRI data were analysed by incorporating the Tofts and Kermode pharmacokinetic model, from which the volume transfer constant (K^{trans}, minute^{-1}), the rate of flux of contrast agent into the extracellular extravascular space within a given volume, was calculated (6).

All data were fitted on a pixel-by-pixel basis using in-house software (ImageView, developed in IDL, ITT Visual Information Systems, Boulder, CO, USA), and the median value of each parameter determined from a ROI that encompassed either the whole brain, whole lesion or a portion of the lesion.

Micro computed tomography

Intact heads from $Hesx1^{Cre/+};Ctnnb1^{lox(ex3)/+}$ mice and wildtype control mice were fixed in 10% formalin for at least 48 hours, and patient-derived xenograft-bearing mouse brains were fixed in 4% formalin, prior to iodination in Lugol's iodine (I^{127} concentration of 2.94×10^{-4}mol/ml) for at least 72 hours to improve tissue contrast. The heads were then rinsed with distilled water to remove excess iodine, blotted dry and secured within a low density plastic container covered with polymer film to prevent specimen dehydration. Images were acquired using a Nikon XTH 225 ST μ-CT scanner, utilising a molybdenum X-ray source with anode voltages ranging between 70-100 kV and detector exposure times of 500-708ms over 3141 projections (2, 14). Data was reconstructed using CTPro3D (Nikon Metrology, Tring) and post-processed with VG Studio MAX software (Volume Graphics GmbH, Heidelberg, Germany).

Histopathology

Formalin-fixed $Hesx1^{Cre/+};Ctnnb1^{lox(ex3)/+}$ mouse tissue imaged by μ-CT was decalcified in 1% formic formaldehyde for 48 hours before embedding in paraffin blocks. A further 5 surface decalcifications of 2 hours each were performed prior to 5μm sections being cut in the axial or sagittal plane, matched to the imaging plane. Sections were then stained with haematoxylin and eosin (H&E).

The brains from patient-derived xenograft-bearing mice were formalin-fixed and processed following μCT imaging, and H&E staining of 3μm axial sections was performed as previously described (26).

Slides were scanned using either Nanozoomer (Hamamatsu Photonics, Welwyn Garden City) or Pannoramic MIDI (3D-Histech, Sysmex Europe) and processed using CaseViewer 2.0 software (3D-Histech, Budapest, Hungary).

Statistics

Statistical and survival analysis was performed with GraphPad Prism 7 (GraphPad Software, La Jolla, USA). The mean of median values for quantitative MRI parameters were reported and used for statistical analysis. Results are presented as the mean $\pm$ 1 standard error of the mean (s.e.m.). Significance testing used Student's unpaired t-test and Pearson correlation coefficient (one tailed) with a 5% confidence level.

Results

***Hesx1^{Cre/+};Ctnnb1^{lox(ex3)/+}* mice develop cystic-solid tumours with a non-linear growth pattern**

MRI and μ-CT imaging performed at 8 weeks of age revealed enlargement of the pituitary of *Hesx1$^{Cre/+}$;Ctnnb1$^{lox(ex3)/+}$* mice relative to wildtype control mice (Figure 1A), consistent with the previously observed prenatal pituitary hyperplasia (11). Serial T_2-weighted MRI performed every 2 weeks revealed a relatively stable phase with no additional changes detectable, followed by lesion enlargement forming a solid tumour with associated cystic fluid accumulation (hyperintense relative to midbrain above; Figure 1B) and in most cases haemorrhage (relatively hypointense).

Tumour progression, defined as a change in imaging phenotype from the stable state, was identified in thirteen *Hesx1$^{Cre/+}$;Ctnnb1$^{lox(ex3)/+}$* mice prior to 1 year of age, at a median age of 17.7 weeks (range 8.3 – 35.3 weeks, n=17) (Figure 1C). Median overall survival in the cohort was found to be 22.6 weeks (range 10.1 – 41.0 weeks). It was noted that tumours that presented later appeared to progress more slowly, and indeed the age at which progression was identified correlated significantly with the time from progression to sacrifice (Pearson r=0.85, p=0.0002).

Multiparametric MRI reveals radiological features similar to human ACP, which correlate with μ-CT and histology

Multiparametric MRI was used to assess the phenotype of progressing *Hesx1$^{Cre/+}$;Ctnnb1$^{lox(ex3)/+}$* tumours. Considerable heterogeneity of cystic components, identified by high T_2-weighted signal intensity, was noted both within and between tumours. In a subset of tumours (n=5) these cysts remained hyperintense on FLAIR images, in which the signal from cerebrospinal fluid (CSF) and other motile fluid compartments would usually be suppressed, and were also relatively hyperintense on T_1-weighted images (Figure 2A left panel, arrow). In another subset (n=5) cystic fluid attenuated to the same degree as ventricular CSF on FLAIR and was isointense to the midbrain on T_1-weighted images (Figure 2A, centre panel, arrowhead). Both of these cystic phenotypes were also identified

within individual lesions (n=3. Figure 2A right panel) and were consistent with the imaging features of the cysts observed in human ACP patients (10).

Quantitative functional MRI incorporating native and contrast-enhanced parameters was also performed at study end. Parametric ADC maps demonstrated that whilst the solid tumour component appeared to have a similar ADC to the rest of the brain (Figure 2B), there was substantial heterogeneity in the tumours corresponding to the different components of the lesions (Figure 2B and 2C). Quantification of ADC in eight end-stage tumours that consisted of all three tumour components showed that ADC was lowest in the solid component ($635\pm29\mathrm{x}10^{-6}\mathrm{mm}^2\mathrm{s}^{-1}$), was significantly higher in the haemorrhagic component ($856\pm79\mathrm{x}10^{-6}\mathrm{mm}^2\mathrm{s}^{-1}$, p=0.02) and was higher still in the cystic regions ($1953\pm73\mathrm{x}10^{-6}\mathrm{mm}^2\mathrm{s}^{-1}$, p<0.0001 vs solid and haemorrhagic).

The uptake and distribution of Gd-DTPA contrast agent in the tumours was assessed using two techniques. T_1-weighted images acquired prior to and following contrast agent administration provided qualitative data that showed heterogeneous signal enhancement in the solid tumour component but no response in the cystic or haemorrhagic components (Figure 2B). Quantitative maps of the transfer coefficient K^{trans} (Figure 2C), which here represents a compound biomarker of perfusion and permeability, demonstrated heterogeneous distribution in the solid tumour component.

Ex vivo μ-CT images of intact tumour-bearing *Hesx1*$^{Cre/+}$*;Ctnnb1*$^{lox(ex3)/+}$ mouse heads, which had been imaged *in vivo* by MRI prior to necropsy, provided higher resolution 3D visualisation of the tumours *in situ*, confirming the complex architecture observed on MRI in addition to more detailed evaluation of microcystic components within the solid tumour (Figure 3 and Supplementary videos 1 and 2). No invasion of the brain parenchyma by the tumour was evident, and whilst smaller cysts within the solid tumour mass were preserved, the integrity of the larger cysts was in some cases

difficult to assess because tissue shrinkage during fixation separated the tumour from the brain. H&E stained sections of the decalcified heads showed clinically relevant histological features observed by MRI and µ-CT; for example densely cellular areas of solid tumour, cysts containing proteinaceous fluid and/or red blood cells, and cyst walls made up of a simple epithelial layer (Figure 3).

Micro-CT imaging of patient-derived ACP xenografts reveals the 3D tumour structure and histological features of human ACP

MRI performed between 124 and 130 days after implantation of uncultured ACP tumour tissue into the cerebral hemisphere of nude mice demonstrated successful engraftment, with tumours appearing heterogeneous on both T_2-weighted and post-contrast T_1-weighted images (Figure 4). *Ex vivo* µ-CT of tumour-bearing brains revealed heterogeneous tumours displaying imaging features that corresponded to histological features commonly observed in human ACP, such as palisading epithelium, epithelial whorls, stellate reticulum, wet keratin and calcification (Figure 4 and Supplementary videos 3, 4 and 5). These features were observed to varying degrees in each of the xenografts.

Discussion

The relevance of preclinical tumour models to human cancer has been a topic of debate for many years. Transgenic models, in which expression or knockout of a specific gene in the native tissue of origin leads to spontaneously arising tumours, orthotopic xenografts, where cancer cells are implanted in the organ from which they originated, and patient-derived xenografts (PDXs), in which human tumour tissue is implanted directly from surgical or biopsy samples, are increasingly being exploited. The use of these models for preclinical cancer research must be underpinned by case-specific evidence for each model establishing that tumour development, progression and radiology recapitulates the human disease. In this study we have used longitudinal *in vivo* MRI and high resolution *ex vivo* μ-CT to compare and contrast the growth patterns and radiological features of tumours arising in $Hesx1^{Cre/+};Ctnnb1^{lox(ex3)/+}$ transgenic mice and in cerebrally implanted patient-derived ACP xenografts.

MRI was first performed when $Hesx1^{Cre/+};Ctnnb1^{lox(ex3)/+}$ mice were approximately 8 weeks of age, where expansion and increased heterogeneity of the pituitary was observed in comparison with wildtype control mice. Due to the size of the mouse pituitary (~1mm x 1mm x 3mm) and the resolution achievable with *in vivo* MRI, it was not possible to detect the microscopic structural changes previously described, which were observed *in utero* as early as 9.5 days post coitum (11). Micro-CT provided a method for high resolution *in situ* imaging, achieving resolution of ~9μm^3, and identified altered architecture of the anterior pituitary and also the posterior lobe of the gland. The high radiation exposure required to acquire images at this resolution and tissue contrast prohibits the use of this protocol *in vivo* and thus for longitudinal studies.

Anatomical T$_2$-weighted MRI provides a non-invasive, non-ionising method of monitoring tumour growth over extended periods of time. In addition, advanced MRI techniques provide a means of

13

defining non-invasive quantitative biomarkers to inform on biologically relevant structure-function relationships in tumours (5). Serial imaging of $Hesx1^{Cre/+};Ctnnb1^{lox(ex3)/+}$ mice revealed that, whilst the pituitary was enlarged from early postnatal life, there was indistinguishable growth during a stable period prior to progression, in some cases rapid, involving solid tumour growth, cystic expansion and other MRI detectable changes. Progressing tumours were identified from 8.3 to 35.3 weeks old (median 17.7 weeks), with 4/17 animals not demonstrating any imaging changes before 1 year of age. Overall survival therefore also differed greatly across the cohort with median survival being 22.6 weeks (4/17 animals alive beyond 1 year of age), considerably longer than the previously reported median survival of 11 weeks, with all animals dying before 6 months of age (11). These differences are likely the consequence of variations in the genetic background since the original study was performed. The time over which tumours progressed was also variable but we show that the age at which tumour progression was identified positively correlated with the time from progression to sacrifice; tumours that took longer to progress from the steady state, also progressed slower once expansion was identified. The molecular mechanisms underpinning this pattern of tumour evolution require further elucidation.

The formation of cysts is a hallmark in the presentation of ACP in children (19) and was observed during necropsy in the $Hesx1^{Cre/+};Ctnnb1^{lox(ex3)/+}$ model (11). Here, we show that the proportion of cystic component varies between tumours, ranging from microcysts within a largely solid lesion, to cysts making up approximately 70% of the abnormality. Most interestingly, in approximately half of the tumours analysed some or all of these cysts appeared hyperintense on FLAIR images and T_1-weighted images, as is often observed in human ACP (10). This is thought to be caused by the presence of high levels of protein, cholesterol and blood breakdown products in the cystic fluid (1, 10, 12), contributing to its description as 'engine oil'. Diffusion-weighed MRI showed that the ADC of the cystic regions was significantly higher than the other regions of the tumours, demonstrating their fluid-filled nature, and ADC values were indistinguishable between cysts that

attenuated on FLAIR images and those that remained hyperintense. Diffusion-weighted MRI has been investigated, alongside MR spectroscopy, for the evaluation of ACP in the clinic (25). Calcification of cyst walls, which is detectable by CT in patients and is integral in the differential diagnosis of ACP (29), was not observed in $Hesx1^{Cre/+};Ctnnb1^{lox(ex3)/+}$ tumours by *ex vivo* μ-CT, which may be related to the relatively short evolution time of mouse tumours compared to human tumours.

The solid component of the tumours, which in some cases did not enlarge far beyond the original size of the abnormal pituitary, were in themselves heterogeneous with small areas of hypointensity on T_2-weighted MRI and evidence of microcysts in some cases. These smaller cysts were also apparent on μ-CT and histologically, consistent with some human ACPs (22). As expected, these regions displayed the most restricted diffusion of water molecules, demonstrating ADC values equivalent to those measured in the normal mouse striatum and intracranially implanted murine tumours (5, 23). Gadolinium contrast agent extravasation occurred heterogeneously in the solid portion of the tumour only, recapitulating the pattern of enhancement in patient tumours (10). In patients, some rim enhancement in the cysts occurs; this was not observed preclinically but may be a feature of the relatively smaller tumours and relatively lower resolution. Imaging and pathological evidence showed that, unlike in patients, the tumours that develop in $Hesx1^{Cre/+};Ctnnb1^{lox(ex3)/+}$ mice do not invade into the brain, which is likely to be as a result of differences in the hypothalamo-pituitary axis anatomy between mice and humans (18).

The majority of mice (11/13) presented with regions of hypointensity on T_2-weighted images, which were either hypointense or isointense with the brain parenchyma on T_1-weighted images, and thus consistent with the presence of paramagnetic species, such as deoxyhaemoglobin, ferritin and hemosiderin, from the blood and degradation of erythrocytes associated with haemorrhage. The size of these regions varied in size up to approximately 70% of the lesion volume in the most extreme

case. ADC in these regions was significantly higher than in the solid component of the tumours but was approximately 2.4 fold lower than the fluid in the cysts, suggesting that there are substantial barriers to the diffusion of water molecules in these regions. Haemorrhage was also identifiable on μ-CT images and H&E staining. The combination of cystic volume and large haemorrhagic regions, leading to raised intracranial pressure, was likely the predominant cause of morbidity in the mouse cohort.

Patient-derived ACP xenografts also showed MRI features similar to human ACP, consistent with the initial description of the model (26). In addition, μ-CT gave further 3D insight into the architecture of these tumours, and highlighted several features of human ACP, including calcification and specific histological structures such as stellate reticulum, wet keratin and palisading epithelium (Figure 4).

As druggable targets are increasingly identified in human and mouse studies (reviewed in (3)) it will be important to develop appropriate preclinical strategies to test novel therapeutic agents. The two models described here are complementary and recapitulate many of the radiological and pathological aspects of human ACP. We anticipate that the use of these murine ACP models will improve the accuracy of preclinical data and accelerate the development of urgently required targeted therapies for these devastating human tumours.

Acknowledgements

References

1. Ahmadi J, Destian S, Apuzzo ML, Segall HD, Zee CS (1992) Cystic fluid in craniopharyngiomas: MR imaging and quantitative analysis. Radiology 182:783-785.

2. Apps JR, Hutchinson JC, Arthurs OJ, Virasami A, Joshi A, Zeller-Plumhoff B, Moulding D, Jacques TS, Sebire NJ, Martinez-Barbera JP (2016) Imaging Invasion: Micro-CT imaging of adamantinomatous craniopharyngioma highlights cell type specific spatial relationships of tissue invasion. Acta Neuropathol Commun 4:57.

3. Apps JR, Martinez-Barbera JP (2016) Molecular pathology of adamantinomatous craniopharyngioma: review and opportunities for practice. Neurosurg Focus 41:E4.

4. Baker LC, Boult JK, Thomas M, Koehler A, Nayak T, Tessier J, Ooi CH, Birzele F, Belousov A, Zajac M, Horn C, LeFave C, Robinson SP (2016) Acute tumour response to a bispecific Ang-2-VEGF-A antibody: insights from multiparametric MRI and gene expression profiling. Br J Cancer 115:691-702.

5. Boult JK, Borri M, Jury A, Popov S, Box G, Perryman L, Eccles SA, Jones C, Robinson SP (2016) Investigating intracranial tumour growth patterns with multiparametric MRI incorporating Gd-DTPA and USPIO-enhanced imaging. NMR Biomed 29:1608-1617.

6. Boult JK, Walker-Samuel S, Jamin Y, Leiper JM, Whitley GS, Robinson SP (2011) Active site mutant dimethylarginine dimethylaminohydrolase 1 expression confers an intermediate tumour phenotype in C6 gliomas. J Pathol 225:344-352.

7. Brastianos PK, Taylor-Weiner A, Manley PE, Jones RT, Dias-Santagata D, Thorner AR, Lawrence MS, Rodriguez FJ, Bernardo LA, Schubert L, Sunkavalli A, Shillingford N, Calicchio ML, Lidov HG, Taha H, Martinez-Lage M, Santi M, Storm PB, Lee JY, Palmer JN, Adappa ND, Scott RM, Dunn IF, Laws ER, Jr., Stewart C, Ligon KL, Hoang MP, Van Hummelen P, Hahn WC, Louis DN, Resnick AC, Kieran MW, Getz G, Santagata S (2014) Exome sequencing identifies BRAF mutations in papillary craniopharyngiomas. Nat Genet 46:161-165.

8. Burghaus S, Holsken A, Buchfelder M, Fahlbusch R, Riederer BM, Hans V, Blumcke I, Buslei R (2010) A tumor-specific cellular environment at the brain invasion border of adamantinomatous craniopharyngiomas. Virchows Arch 456:287-300.

9. Buslei R, Nolde M, Hofmann B, Meissner S, Eyupoglu IY, Siebzehnrubl F, Hahnen E, Kreutzer J, Fahlbusch R (2005) Common mutations of beta-catenin in adamantinomatous craniopharyngiomas but not in other tumours originating from the sellar region. Acta Neuropathol 109:589-597.

10. Curran JG, O'Connor E (2005) Imaging of craniopharyngioma. Childs Nerv Syst 21:635-639.

11. Gaston-Massuet C, Andoniadou CL, Signore M, Jayakody SA, Charolidi N, Kyeyune R, Vernay B, Jacques TS, Taketo MM, Le Tissier P, Dattani MT, Martinez-Barbera JP (2011) Increased Wingless (Wnt) signaling in pituitary progenitor/stem cells gives rise to pituitary tumors in mice and humans. Proc Natl Acad Sci U S A 108:11482-11487.

12. Haghighatkhah HR, Taheri MS, Haghighi M, Shahzadi S, Birang S (2010) Imaging of Monstrous Craniopharyngioma: A Pictorial Essay. Iranian Journal of Radiology 7:79-89.

13. Holsken A, Sill M, Merkle J, Schweizer L, Buchfelder M, Flitsch J, Fahlbusch R, Metzler M, Kool M, Pfister SM, von Deimling A, Capper D, Jones DT, Buslei R (2016) Adamantinomatous and papillary craniopharyngiomas are characterized by distinct epigenomic as well as mutational and transcriptomic profiles. Acta Neuropathol Commun 4:20.

14. Hutchinson JC, Arthurs OJ, Ashworth MT, Ramsey AT, Mifsud W, Lombardi CM, Sebire NJ (2016) Clinical utility of postmortem microcomputed tomography of the fetal heart: diagnostic imaging vs macroscopic dissection. Ultrasound Obstet Gynecol 47:58-64.

15. Kato K, Nakatani Y, Kanno H, Inayama Y, Ijiri R, Nagahara N, Miyake T, Tanaka M, Ito Y, Aida N, Tachibana K, Sekido K, Tanaka Y (2004) Possible linkage between specific histological structures and aberrant reactivation of the Wnt pathway in adamantinomatous craniopharyngioma. The Journal of pathology 203:814-821.

16. Kilkenny C, Browne WJ, Cuthill IC, Emerson M, Altman DG (2010) Improving bioscience research reporting: the ARRIVE guidelines for reporting animal research. PLoS Biol 8:e1000412.

17. Louis DN, Perry A, Reifenberger G, von Deimling A, Figarella-Branger D, Cavenee WK, Ohgaki H, Wiestler OD, Kleihues P, Ellison DW (2016) The 2016 World Health Organization Classification of Tumors of the Central Nervous System: a summary. Acta Neuropathol 131:803-820.

18. Martinez-Barbera JP (2015) 60 YEARS OF NEUROENDOCRINOLOGY: Biology of human craniopharyngioma: lessons from mouse models. J Endocrinol 226:T161-172.

19. Martinez-Barbera JP, Buslei R (2015) Adamantinomatous craniopharyngioma: pathology, molecular genetics and mouse models. J Pediatr Endocrinol Metab 28:7-17.

20. Muller HL (2010) Childhood craniopharyngioma--current concepts in diagnosis, therapy and follow-up. Nat Rev Endocrinol 6:609-618.

21. Nielsen EH, Feldt-Rasmussen U, Poulsgaard L, Kristensen LO, Astrup J, Jorgensen JO, Bjerre P, Andersen M, Andersen C, Jorgensen J, Lindholm J, Laurberg P (2011) Incidence of craniopharyngioma in Denmark (n = 189) and estimated world incidence of craniopharyngioma in children and adults. J Neurooncol 104:755-763.

22. Paulus W, Stockel C, Krauss J, Sorensen N, Roggendorf W (1997) Odontogenic classification of craniopharyngiomas: a clinicopathological study of 54 cases. Histopathology 30:172-176.

23. Rau PR, Sellner J, Heiland S, Plaschke K, Schellinger PD, Meyding-Lamade UK, Lamade WR (2006) Apparent diffusion coefficient in the aging mouse brain: a magnetic resonance imaging study. Life Sci 78:1175-1180.

24. Sekine S, Sato S, Takata T, Fukuda Y, Ishida T, Kishino M, Shibata T, Kanai Y, Hirohashi S (2003) Beta-catenin mutations are frequent in calcifying odontogenic cysts, but rare in ameloblastomas. Am J Pathol 163:1707-1712.

25. Sener RN (2001) Proton MR spectroscopy of craniopharyngiomas. Comput Med Imaging Graph 25:417-422.

26. Stache C, Holsken A, Schlaffer SM, Hess A, Metzler M, Frey B, Fahlbusch R, Flitsch J, Buchfelder M, Buslei R (2015) Insights into the infiltrative behavior of adamantinomatous craniopharyngioma in a new xenotransplant mouse model. Brain Pathol 25:1-10.

27. Walker-Samuel S, Orton M, Boult JK, Robinson SP (2011) Improving apparent diffusion coefficient estimates and elucidating tumor heterogeneity using Bayesian adaptive smoothing. Magn Reson Med 65:438-447.

28. Walker-Samuel S, Orton M, McPhail LD, Boult JK, Box G, Eccles SA, Robinson SP (2010) Bayesian estimation of changes in transverse relaxation rates. Magn Reson Med 64:914-921.

29. Warmuth-Metz M, Gnekow AK, Muller H, Solymosi L (2004) Differential diagnosis of suprasellar tumors in children. Klin Padiatr 216:323-330.

30. Workman P, Aboagye E, Balkwill F, Balmain A, Bruder G, Chaplin D, Double J, Everitt J, Farningham D, Glennie M, Kelland L, Robinson V, Stratford I, Tozer G, Watson S, Wedge S, Eccles S, Navaratnam V, Ryder S, Institute CotNCR (2010) Guidelines for the welfare and use of animals in cancer research. Br J Cancer 102:1555-1577.

Figure Legends

Figure 1

A. Axial *in vivo* T_2-weighted MRI (upper panel) and *ex vivo* micro (μ)-CT (lower panel) images of the pituitary region of 8 week old control and *Hesx1$^{Cre/+}$;Ctnnb1$^{lox(ex3)/+}$* mutant mice (each image acquired from a different mouse). Note the expansion and increased heterogeneity of the *Hesx1$^{Cre/+}$;Ctnnb1$^{lox(ex3)/+}$* pituitaries (solid arrows) relative to the controls (dashed arrows). Arrowheads indicate the posterior lobe of pituitary also detectable in μ-CT images and * denotes the sphenoid bone in control mice. MRI resolution 98x98x1000μm; μ-CT resolution approximately 9μm isotropic. **B.** T_2-weighted MRI images of a *Hesx1$^{Cre/+}$;Ctnnb1$^{lox(ex3)/+}$* mouse demonstrating the evolution of a tumour. In this mouse the first remarkable change was detected at 17.7 weeks, which was followed by rapid tumour progression including growth of the solid component, cyst formation and haemorrhage; the mouse was humanely killed at 22.6 weeks according to Home Office regulations. **C.** Progression-free and overall survival curves to 1 year of age representing data from seventeen *Hesx1$^{Cre/+}$;Ctnnb1$^{lox(ex3)/+}$* mice alongside the correlation between time to tumour identification and time between identification of tumour and death for twelve animals. Pearson correlation coefficient and one tailed significance analysis.

Figure 2

A. T_2-weighted (T_2-w), fluid attenuated inversion recovery (FLAIR) and T_1-weighted (T_1-w) MRI images from three *Hesx1$^{Cre/+}$;Ctnnb1$^{lox(ex3)/+}$* mice demonstrating different cyst imaging presentation. Arrows denote cystic fluid that did not attenuate on FLAIR and was hyperintense on T_1-weighted MRI; arrowheads denote cystic fluid that attenuated on FLAIR and was isointense on T_1-weighted MRI. The example on the right shows both cyst phenotypes in the same tumour. **B. Upper panel:** T_2-weighted and FLAIR images, and a parametric map of apparent diffusion coefficient (ADC) acquired from a 1mm thick axial slice through a tumour-bearing

Hesx1$^{Cre/+}$*;Ctnnb1*$^{lox(ex3)/+}$ mouse head. **Lower panel:** Matched T$_1$-weighted images acquired at baseline and 1 minute after injection of 0.1mmol/kg Gd-DTPA and a subtraction map clearly showing areas of signal enhancement. Green ROI denotes lesion volume. **C.** Parametric maps of ADC and transfer coefficient K^{trans} in the entire lesion and the solid component of a *Hesx1*$^{Cre/+}$*;Ctnnb1*$^{lox(ex3)/+}$ tumour alongside a T$_2$-weighted anatomical image of the matched 1mm slice. Green ROI denotes solid component of the lesion. Note the heterogeneous signal enhancement in the solid tumour components following contrast administration and high ADC in cystic areas in B and C.

Figure 3

In vivo T$_2$-weighted MRI, *ex vivo* micro (μ)-CT and H&E stained sections from two tumour-bearing *Hesx1*$^{Cre/+}$*;Ctnnb1*$^{lox(ex3)/+}$ mouse heads. Snapshots of H&E staining were acquired at x100 (upper panel) and x400 (lower panel) magnification. Arrow denotes densely cellular solid tumour. Small cysts contained proteinaceous fluid (+) and/or red blood cells (*). Arrowhead indicates the simple epithelial layer that made up the wall of a large cyst. MRI slice thickness 1000μm, μ-CT slice thickness ≈ 9μm, tissue sections 5μm.

Figure 4

In vivo T$_2$-weighted and gadobutrol-enhanced T$_1$-weighted MRI acquired immediately prior to necropsy, *ex vivo* micro (μ)-CT and H&E stained sections from three mice bearing cerebrally-implanted patient-derived ACP xenografts. Histological features from the patient's tumour were maintained; cell clusters (#) palisading epithelium (arrowhead), stellate reticulum (*), calcification (arrows) and wet keratin (+). MRI slice thickness 700μm, μ-CT slice thickness ≈ 4-6μm, tissue sections 3μm.

Supplementary Material Legends

Supplementary Video 1

Micro-CT volume rendering (isotropic voxel size=9.1µm) demonstrating virtual dissection of the tumour that arose in the *Hesx1*$^{Cre/+}$*;Ctnnb1*$^{lox(ex3)/+}$ mouse shown in the upper panel of Figure 3. Complex areas of cystic and solid tumour can be identified, along with compression of the surrounding brain parenchyma.

Supplementary Video 2

Micro-CT volume rendering (isotropic voxel size=8.7µm) demonstrating virtual dissection of the tumour that arose in the *Hesx1*$^{Cre/+}$*;Ctnnb1*$^{lox(ex3)/+}$ mouse shown in the lower panel of Figure 3. Complex areas of cystic and solid tumour can be identified, along with compression of the surrounding brain parenchyma.
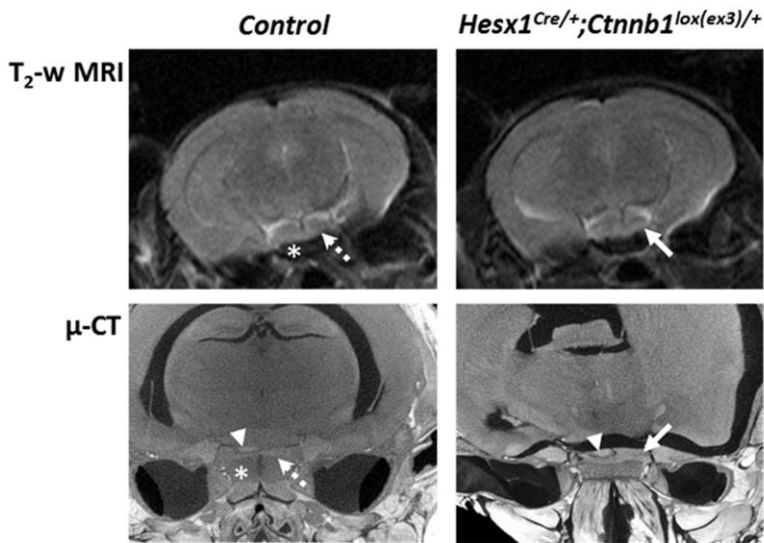
Supplementary Video 3

Micro-CT volume rendering (isotropic voxel size=3.7µm) demonstrating virtual dissection of the cerebrally-implanted patient-derived ACP xenograft shown in the upper panel of Figure 4. High spatial resolution and differential uptake of iodine-based contrast enables visualisation of a cluster within an area of stellate reticulum.

Supplementary Video 4

Micro-CT volume rendering (isotropic voxel size=6.1µm) demonstrating virtual dissection of the cerebrally-implanted patient-derived ACP xenograft shown in the middle panel of Figure 4. A radio-dense focus can be seen within the xenograft; this corresponds to an area of calcification on histological examination.
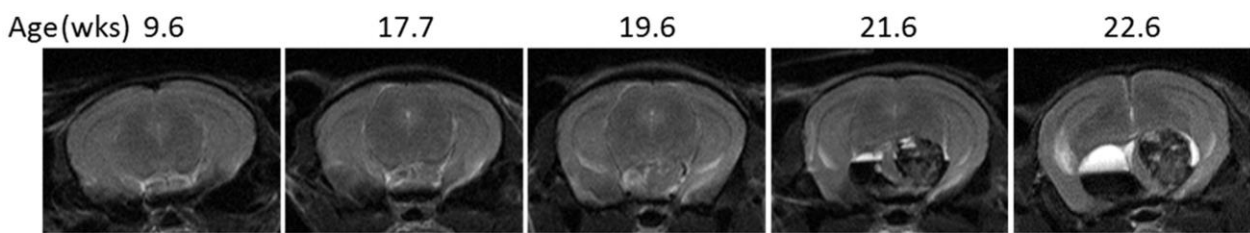
Supplementary Video 5

Micro-CT volume rendering (isotropic voxel size=3.8μm) demonstrating virtual dissection of the cerebrally-implanted patient-derived ACP xenograft shown in the lower panel of Figure 4. Islands of wet keratin adjacent to solid tumour (confirmed on H&E, Figure 4) give the xenograft a heterogeneous appearance on micro-CT examination.
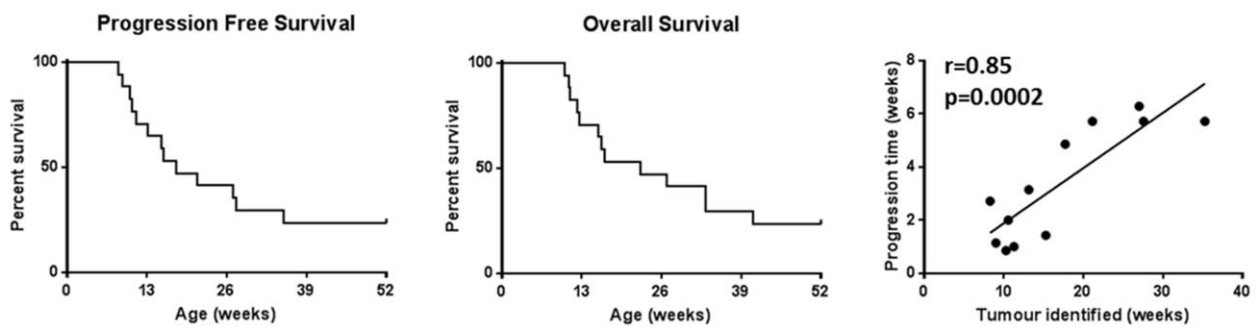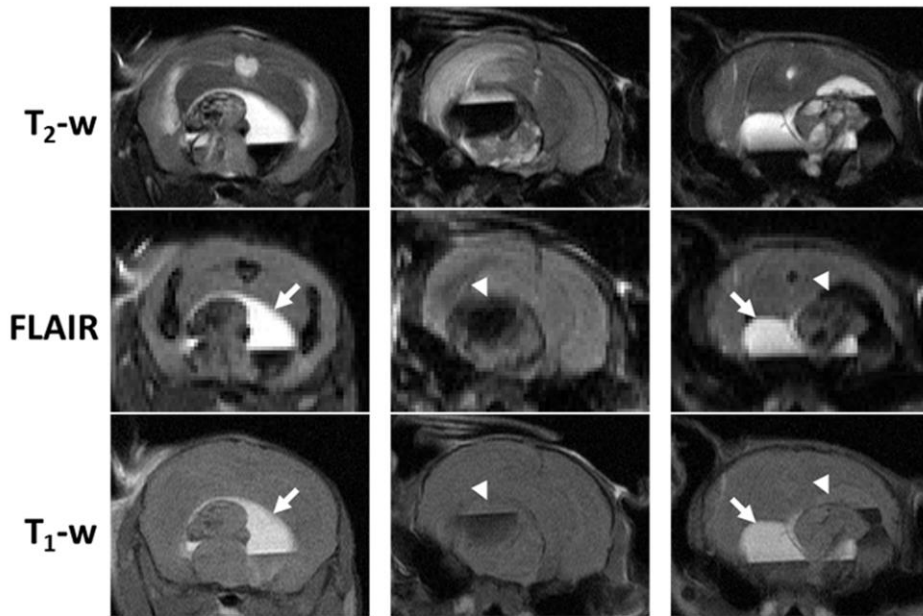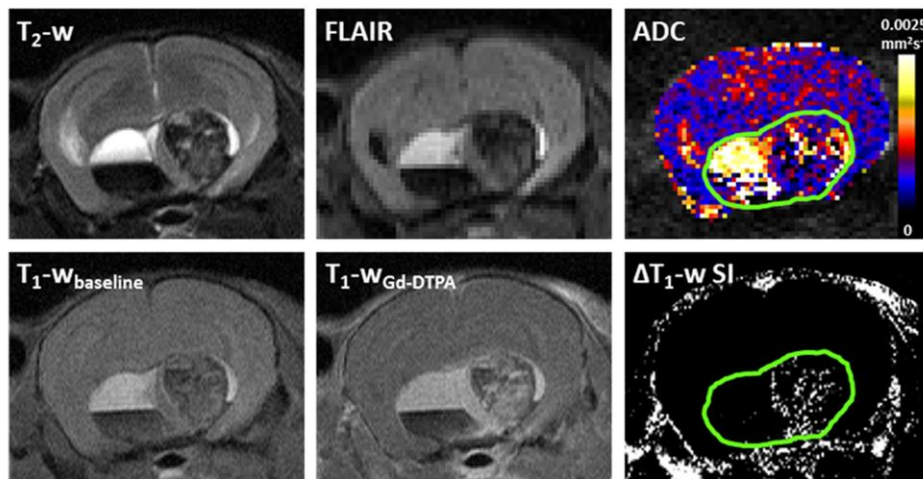
Figure 1

A

	Control	*Hesx1$^{Cre/+}$;Ctnnb1$^{lox(ex3)/+}$*
T$_2$-w MRI		
μ-CT		

B

Age (wks) 9.6   17.7   19.6   21.6   22.6

C

Progression Free Survival

Overall Survival

r=0.85
p=0.0002

Figure 2

A

B

C

Figure 3

Figure 4